



Integration of adsorption and photosensitivity capabilities into a cationic multivariate metal-organic framework for enhanced visible-light photoreduction reaction



Xu-Sheng Wang^{a,b,c}, Chun-Hui Chen^a, Fumihiko Ichihara^{c,d}, Mitsutake Oshikiri^c, Jun Liang^a, Lan Li^{a,b}, Yunxiang Li^{c,d}, Hui Song^{c,d}, Shengyao Wang^c, Teng Zhang^a, Yuan-Biao Huang^{a,b,*}, Rong Cao^{a,b,*}, Jinhua Ye^{c,d,e,f,*}

^a State Key Laboratory of Structural Chemistry, Fujian Institute of Research on the Structure of Matter (FJIRSM), Chinese Academy of Sciences (CAS), Fuzhou, Fujian, 350002, PR China

^b University of the Chinese Academy of Sciences (UCAS), Beijing, 100049, PR China

^c International Center for Materials Nanoarchitectonics (WPI-MANA), National Institute for Materials Science (NIMS), 1-1 Namiki, Tsukuba, 305-0047, Japan

^d Graduate School of Chemical Sciences and Engineering, Hokkaido University, Sapporo, 060-0814, Japan

^e TJU-NIMS International Collaboration Laboratory, School of Material Science and Engineering, Tianjin University, Tianjin, 300072, PR China

^f Collaborative Innovation Center of Chemical Science and Engineering (Tianjin), Tianjin, 300072, PR China

ARTICLE INFO

Keywords:

Photocatalysis
Multivariate metal-organic frameworks
Cr(VI) adsorption
Photosensitive unit
Cationic framework

ABSTRACT

The photoreduction of toxic Cr(VI) to environmental Cr(III) driven by visible-light is highly desired. Metal-organic frameworks (MOFs), as one class of outstanding porous materials, had been utilized for photoreduction of Cr(VI). Current methods modulated the photoreduction of Cr(VI) mainly by selection of suitable metal ions or organic ligands in single component MOFs. However, most of them still exhibit limited photoreduction performance due to low Cr(VI) adsorption rate/capacity, weak light harvesting efficiency, and/or poor electronic utilization efficiency. Multivariate metal-organic frameworks with highly visible-light photosensitive unit and strong Cr(VI) adsorption strut into one single phase is therefore expected to be an effective strategy to improve the photoreduction of Cr(VI), but remains unexplored. Herein, intense visible-light absorption porphyrin unit and strong toxic anions adsorption strut were integrated into one single MOF simultaneously via a sequential mixed-ligand and ionization method, which strongly improve the photoreduction performance of Cr(VI). The synergistic effect of strong adsorption of $\text{Cr}_2\text{O}_7^{2-}$ and efficient utilization of light endowed $\text{H}_2\text{TCPP} \subset (\text{I}-)\text{Meim-UiO-66}$ with highly efficient photoreduction activity toward toxic $\text{Cr}_2\text{O}_7^{2-}$ under visible light in a rate of 13.3 mg_{Cr(VI)}/g_{catalyst}/min, much higher than the reported MOF-based photocatalysts including typical NH₂-UiO-66 (0.2 mg_{Cr(VI)}/g_{catalyst}/min) and NH₂-MIL-125 (1.6 mg_{Cr(VI)}/g_{catalyst}/min). As far as we know, this is the best catalyst among all the reported MOF-based photocatalysts for Cr(VI) photoreduction, in which the I- in our imidazolium functionalized MOF acts as sacrificial agent. Based on the results from time-resolved photoluminescence spectra, electron spin resonance, and theoretical calculation etc., a photoreduction mechanism of $\text{Cr}_2\text{O}_7^{2-}$ over $\text{H}_2\text{TCPP} \subset (\text{I}-)\text{Meim-UiO-66}$ was also well proposed. This general and facial strategy, combining the advantages of adsorption and photosensitivity in a multivariate MOF, paves the way to design of higher efficient photocatalytic materials.

1. Introduction

Cr(VI) ion, as one of the most toxic heavy metal ions in waste water, can cause severe damage to organisms, even in very low doses [1]. To date, many techniques, including ion exchange, chemical precipitation,

membrane filtration, reverse osmosis, adsorption, and reduction of Cr(VI) to low toxicity Cr(III), have been applied for the removal of Cr(VI) [2]. Among these techniques, the reduction of Cr(VI) to Cr(III) is one of the most promising techniques because low-toxicity Cr(III) can be easily recovered and utilized for other applications [2]. In comparison with

* Corresponding authors at: State Key Laboratory of Structural Chemistry, Fujian Institute of Research on the Structure of Matter (FJIRSM), Chinese Academy of Sciences (CAS), Fuzhou, Fujian, 350002, PR China.

E-mail addresses: ybhuang@fjirsm.ac.cn (Y.-B. Huang), rcao@fjirsm.ac.cn (R. Cao), Jinhua.YE@nims.go.jp (J. Ye).

the traditional chemical reduction approaches, the photoreduction of Cr(VI) to Cr(III) driven by visible-light is an energy-efficient and environmentally friendly approach [3–5]. However, most photocatalysts, including TiO₂- and ZnO-based catalysts, exhibit limited reduction performance due to their poor Cr(VI) adsorption and narrow visible-light adsorption range [6–8]. Therefore, it is necessary to design and prepare highly efficient photocatalysts with large Cr(VI) adsorption uptake and wide visible-light absorption ranges for the photoreduction of Cr(VI) to Cr(III).

Over the past two decades, metal-organic frameworks (MOFs), as one class of outstanding porous materials, have been widely utilized for gas capture and separation, catalysis, and detection due to their high pore volume and surface area as well as their adjustable structures and functions [9–16]. Particularly, the presence of tunable functional organic linkers and transition metal centers in MOFs could make them act as promising semiconductor-like porous photocatalysts via ligand-to-metal charge transfer (LMCT), metal-to-ligand charge transfer (MLCT), or π - π^* transition of the delocalized linker, etc [17–19]. However, only a handful of MOFs have been utilized for the photoreduction of Cr(VI) to Cr(III) with unsatisfied photocatalytic activity so far due to the low adsorption rate/capacity of Cr(VI) and narrow light adsorption range, etc [7,8,20–26]. Multivariate metal-organic frameworks with multiple functionalities in one single phase are of great interest for gas adsorption and catalysis [27–30]. The simultaneous integration of highly visible-light photosensitive units and strong Cr(VI) adsorptive cationic struts into a multivariate MOF is therefore expected to be an effective strategy to improve the photoreduction of Cr(VI), but remains unexplored.

Herein, a multivariate MOF, H₂TCPP \subset (I[−])Meim-Uio-66 (where H₂TCPP, I[−], Me, and im stand for tetrakis (4-carboxyphenyl) porphyrin, iodide ion, methyl, and imidazolium), with the integration of intense visible-light absorption porphyrin unit and strong Cr₂O₇^{2−} adsorption cationic strut, was fabricated via a sequential mixed-ligand and ionization strategy (Fig. 1a). Porphyrin, acting as intense visible-light photosensitive unit, was firstly integrated into an imidazole-functionalized Zr-based MOF by a mixed-ligand strategy, which effectively expanded the spectral response from 425 to 750 nm [29–31]. Considering that the existing species of Cr(VI) and Cr(III) are Cr₂O₇^{2−} and Cr³⁺ in acidic water, respectively, hydrophilic cationic MOFs could promote the adsorption of anionic Cr₂O₇^{2−} and the desorption of the reduced cationic Cr³⁺ due to the electrostatic effect [32]. Thus, the porphyrin incorporated H₂TCPP \subset Im-Uio-66 was further ionized by the reaction with methyl iodide to afford the cationic H₂TCPP \subset (I[−])Meim-Uio-66 (I[−] as mobile counter anion), which could enhance the adsorption of Cr₂O₇^{2−} through ion exchange mechanism. Thus, the co-operation between the strong adsorption of Cr₂O₇^{2−} and the efficient absorption of visible-light endowed H₂TCPP \subset (I[−])Meim-Uio-66 with highly efficient photoreduction activity toward Cr₂O₇^{2−} under visible light in a rate of 13.3 mg_{Cr(VI)}/g_{catalyst}/min, much higher than the reported MOF-based photocatalysts including typical NH₂-Uio-66 (0.2 mg_{Cr(VI)}/g_{catalyst}/min) and NH₂-MIL-125 (1.6 mg_{Cr(VI)}/g_{catalyst}/min). This work will open a new avenue for designing highly efficient multifunctional photocatalysts.

2. Experimental

2.1. Materials

All reagents were purchased from commercial sources without further purification, except that Im-H₂BDC-HCl-H₂O (Im-H₂BDC stands for 2-(imidazol-1-yl)terephthalic acid) was prepared according to the literature [33].

2.2. Synthesis of H₂TCPP \subset (I[−])Meim-Uio-66

A sequential mixed-ligand and ionization method was employed to

synthesize the MOF H₂TCPP \subset (I[−])Meim-Uio-66. First, the imidazole functionalized H₂TCPP \subset Im-Uio-66 was synthesized using the mixed-ligand approach. A mixture of ZrCl₄ (25 mg), Im-H₂BDC-HCl-H₂O (30 mg), H₂TCPP (3.5 mg), acetic acid (0.57 mL) and 3 mL of DMF was sonicated sufficiently before being transferred in a 15-mL Pyrex vial. The Pyrex vial was heated in an oven at 120 °C for 12 h. After slowly cooling the reaction to room temperature, the precipitate H₂TCPP \subset Im-Uio-66 was isolated by centrifugation, repeatedly washed with DMF and acetone, and then dried in an oven at 120 °C under vacuum. For the synthesis of the catalyst H₂TCPP \subset (I[−])Meim-Uio-66, a mixture of H₂TCPP \subset Im-Uio-66 (0.2 g) and methyl iodide (1.0 mL) in CH₃CN (15 mL) was heated at 80 °C for 48 h under a N₂ atmosphere. The brown H₂TCPP \subset (I[−])Meim-Uio-66 product was collected by centrifugation and washed with EtOH, acetone, ether and dried at 120 °C under vacuum for 12 h, resulting in the following IR characteristics (KBr, ν_{max} , cm^{−1}): 2960 (w), 2924 (w), 1709 (s), 1597 (s), 1500 (s), 1416 (m), 1392 (s), 1377 (s), 771 (s), 654 (s).

2.3. Physical measurements

N₂ sorption isotherms were measured using a Micrometrics ASAP 2460 instrument at 77 K. Before the measurement, the samples for N₂ sorption were activated at 393 K in vacuum for 10 h. Powder X-ray diffraction patterns (PXRD) were recorded on a Rigaku MiniFlex 600 diffractometer equipped with Cu-K α radiation ($\lambda = 1.54056 \text{ \AA}$) over the 2 θ range of 5–45° with a scan speed of 5° min^{−1} at room temperature. Fourier transform infrared (FT-IR) spectra were recorded on a PerkinElmer Spectrum One in the range of 400–4000 cm^{−1} using KBr pellets. Several milligrams of catalysts were added into the mixture of 500 μ L of DMSO-*d*₆ and 30 μ L of HF and sonicated for several minutes for a later ¹H NMR test. The ¹H NMR was performed with a AVANCE III Bruker Biospin spectrometer (400 MHz). The morphologies of MOF nanoparticles were studied using a scanning electron microscope (SEM) (working at 10 KV). The photoluminescence (PL) spectra were collected with a FS5 Fluorescence Spectrometer. UV-vis adsorption spectra were collected on a Shimadzu UV-2600 spectrophotometer.

2.4. Photoelectrochemical measurement

The photoelectrode was prepared according to the following typical procedure: 5 mg of the MOF sample was added into a mixture of Nafion (20 μ L) and ethanol (2 mL). Then, the obtained suspension (80 μ L) was dropped onto the surface of an ITO plate. The photocatalyst-coated ITO plate was dried in an IR oven for a few minutes. Photocurrent measurements were performed on a workstation (CHI760E) in a standard three-electrode system configuration with the photocatalyst-coated ITO as the working electrode, Pt net as the counter electrode, and Ag/AgCl as the reference electrode. A 300-W xenon lamp was used as the light source for the photocurrent measurement. The photoresponsive signals of the samples were measured under visible light (420 nm–780 nm) at 0.4 V. The measurements for the Mott-Schottky plots of samples were also performed on an electrochemical workstation (IM6ex, Zahner, Germany) in a standard three-electrode system configuration using 0.2 M Na₂SO₄ solution as the electrolyte at frequencies of 100, 500, 1000, and 1500 Hz, respectively.

2.5. Adsorption of Cr₂O₇^{2−}

In a typical procedure, the adsorption of Cr₂O₇^{2−} was carried out in a 200-mL quartz reactor. A total of 10 mg of MOF was added into 40 mL of 100 ppm K₂Cr₂O₇ aqueous solution and stirred in the dark. The pH of the Cr₂O₇^{2−} aqueous solution was adjusted by HCl or NaOH. During the adsorption process, 1 mL of the suspension was taken from the reactor at given time intervals and analyzed by UV-vis spectroscopy using the previously reported diphenylcarbazide (DPC) method [7b,7c]. The detailed experimental procedure was demonstrated as follows: 1 mL of the

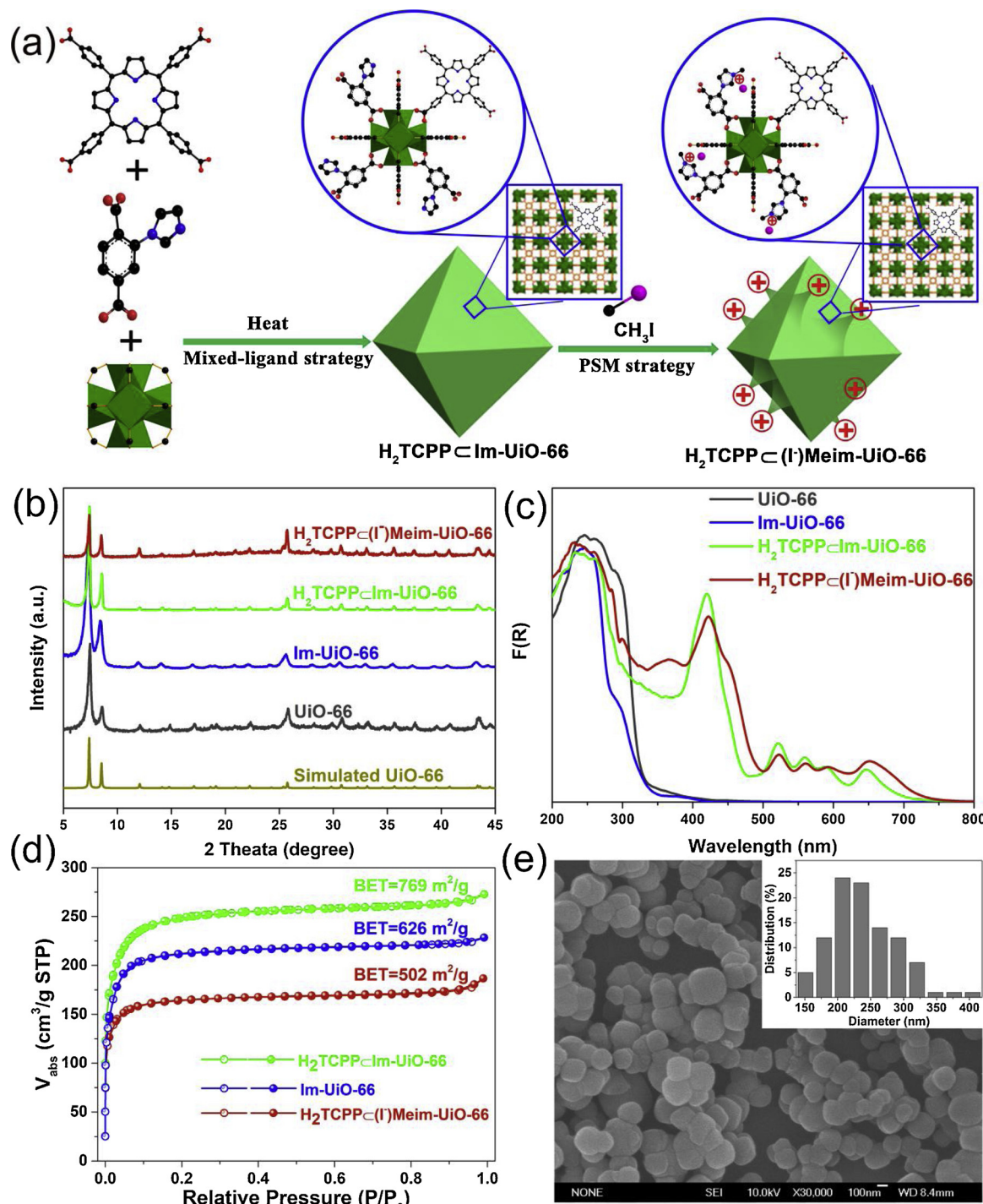


Fig. 1. a) Schematic illustration of the construction process of multivariate $\text{H}_2\text{TCPP} \subset (\text{I}^-)\text{Meim-UiO-66}$. b) The PXRD patterns of the simulated UiO-66 and the as-synthesized UiO-66 , Im-UiO-66 , $\text{H}_2\text{TCPP} \subset \text{Im-UiO-66}$, and $\text{H}_2\text{TCPP} \subset (\text{I}^-)\text{Meim-UiO-66}$. c) The solid UV-vis DRS of UiO-66 , Im-UiO-66 , $\text{H}_2\text{TCPP} \subset \text{Im-UiO-66}$, and $\text{H}_2\text{TCPP} \subset (\text{I}^-)\text{Meim-UiO-66}$. d) The N_2 sorption isotherms of $\text{H}_2\text{TCPP} \subset \text{Im-UiO-66}$, $\text{H}_2\text{TCPP} \subset (\text{I}^-)\text{Meim-UiO-66}$ and Im-UiO-66 . e) The SEM image of $\text{H}_2\text{TCPP} \subset (\text{I}^-)\text{Meim-UiO-66}$ (the inset diagram is the size distribution of $\text{H}_2\text{TCPP} \subset (\text{I}^-)\text{Meim-UiO-66}$).

$\text{Cr}_2\text{O}_7^{2-}$ suspension was treated by a syringe filter to remove the catalyst and added to a mixture of 9 mL of 0.2 M H_2SO_4 solution and 0.2 mL of freshly prepared 0.25% (w/v) DPC acetone solution. After shaking for 30 s, the mixture was allowed to stand for 10 min and then analyzed by UV-vis spectroscopy.

2.6. Photocatalytic experiments

In a typical procedure, the photocatalytic reduction of $\text{Cr}_2\text{O}_7^{2-}$ to

Cr^{3+} was carried out in a 200-mL quartz reactor containing 10 mg of photocatalyst and 40 mL of 100 ppm $\text{Cr}_2\text{O}_7^{2-}$ aqueous solution. The pH of the $\text{Cr}_2\text{O}_7^{2-}$ aqueous solution was adjusted by HCl or NaOH. After the adsorption-desorption equilibrium was completed under stirring in the dark for one hour, the reactor was exposed to visible-light irradiation (a 300-W Xe lamp with a 420-nm cut off filter, 420 nm–780 nm). During the irradiation process, 1 mL of the suspension was taken from the reactor at given time intervals and analyzed by UV-vis spectroscopy using the previously reported diphenylcarbazide (DPC) method. The

detailed experimental procedure is provided as follows: 1 mL of the $\text{Cr}_2\text{O}_7^{2-}$ solution was added to a mixture of 9 mL of 0.2 M H_2SO_4 solution and 0.2 mL of freshly prepared 0.25% (w/v) DPC acetone solution. After shaking for 30 s, the mixture was allowed to stand for 10 min to ensure full color development. Then, the mixture was analyzed by UV-vis spectroscopy. After the photocatalytic reaction, the catalyst was collected by centrifugation and washed by KI solution, water ($\text{pH} = 2$), and ethanol. Finally, the catalyst was dried at 70 °C overnight and applied for the next run.

3. Results and discussion

3.1. Structure characterization of multivariate MOF photocatalyst

The target multivariate MOF, $\text{H}_2\text{TCPP} \subset (\text{I}^-)\text{Meim-UiO-66}$, with the integration of intense visible-light absorption porphyrin unit and strong $\text{Cr}_2\text{O}_7^{2-}$ adsorption cationic strut, was synthesized through a sequential mixed-ligand and PSM strategy (Fig. 1a). To expand the light absorption range of the photocatalyst, the neutral MOF, $\text{H}_2\text{TCPP} \subset \text{Im-UiO-66}$, was initially constructed from the mixed-ligand of 2-(imidazol-1-yl) terephthalic acid (Im-H₂BDC) and H₂TCPP. The content of the incorporated ligand H₂TCPP was determined by ¹H-NMR after digestion by HF (40%) (Fig. S1), which revealed that the molar ratio of Im-H₂BDC and H₂TCPP was ca. 38 : 1. As shown in Fig. 1b, the powder X-ray diffraction (PXRD) demonstrates that the diffraction peaks of the obtained $\text{H}_2\text{TCPP} \subset \text{Im-UiO-66}$ nanocrystals (220 nm, Fig. S2) are in good agreement with the simulated UiO-66 and the imidazole-functionalized Im-UiO-66. [31,33] The result indicated that the incorporation of a small amount of porphyrin units into the framework of Im-UiO-66 did not alter its topological structure [30]. The $\text{H}_2\text{TCPP} \subset \text{Im-UiO-66}$ sample remained light brown after washing with *N,N*-dimethylformamide (DMF) and acetone, which is markedly different from the color (white) of Im-UiO-66, indicating that H₂TCPP ligands have been successfully incorporated into the Im-UiO-66 framework (Fig. S3). Furthermore, the solid UV-vis diffuse reflection spectrum (DRS) of $\text{H}_2\text{TCPP} \subset \text{Im-UiO-66}$ (Fig. 1c) shows the characteristic absorption bands of the porphyrin unit at 420 nm (Soret band) and 500–750 nm (four Q bands), further demonstrating that the ligand H₂TCPP has been successfully incorporated into its framework. It should be noted that the incorporated H₂TCPP was prefer to be coordinated to the Zr₆ nodes, rather than just purely trapped in the pore of MOF [30,34,35]. The successful insertion of porphyrin into MOF was attributed to the fact that the multitopic carboxylic functionalized linker is favoured to be coordinated to Zr₆ nodes. As we expected, compared with that of Im-UiO-66, the introduction of the photosensitive ligands H₂TCPP endows its absorption range extending from 425 nm to 750 nm, which will be beneficial for enhancing photocatalytic activity. Moreover, the N₂ sorption isotherm measurement revealed that $\text{H}_2\text{TCPP} \subset \text{Im-UiO-66}$ has large Brunauer-Emmett-Teller (BET) surface area (769 m²/g) and pore volume (0.42 cm³/g) (Fig. 1d), which will be favorable to the following ionization.

The imidazole-functionalized $\text{H}_2\text{TCPP} \subset \text{Im-UiO-66}$ was further ionized by the reaction with methyl iodide to afford the cationic $\text{H}_2\text{TCPP} \subset (\text{I}^-)\text{Meim-UiO-66}$ (I[−] as mobile counter anion) (Fig. 1a). The same PXRD patterns of $\text{H}_2\text{TCPP} \subset (\text{I}^-)\text{Meim-UiO-66}$ and $\text{H}_2\text{TCPP} \subset \text{Im-UiO-66}$ indicated that the crystallographic phase was retained after ionization (Fig. 1b). Furthermore, decreasing the size of the photocatalyst to the nano level is beneficial for the light absorption and the mass-transfer within the porous structure during the photocatalytic process, thus improving the catalytic performance. Interestingly, as shown in Figs. 1e and S2, the scanning electron microscopy (SEM) images show that the particles sizes of $\text{H}_2\text{TCPP} \subset (\text{I}^-)\text{Meim-UiO-66}$ are similar to the parent $\text{H}_2\text{TCPP} \subset \text{Im-UiO-66}$ with an average size of 220 nm. The solid UV-vis spectrum (Fig. 1c) of $\text{H}_2\text{TCPP} \subset (\text{I}^-)\text{Meim-UiO-66}$ still shows the strong visible absorption bands of porphyrin, revealing that the catalyst is stable and the H₂TCPP ligands were not

dissociated and escaped from the frameworks during the PSM process. Furthermore, after ionization, $\text{H}_2\text{TCPP} \subset (\text{I}^-)\text{Meim-UiO-66}$ still exhibited a high BET surface area of 502 m²/g (Fig. 1d), which is beneficial to the adsorption and photoreduction of $\text{Cr}_2\text{O}_7^{2-}$ to Cr³⁺.

3.2. Evaluation of the photoreduction activity

The $\text{Cr}_2\text{O}_7^{2-}$ anions adsorption performance by photocatalysts is vital for their photoreduction. Therefore, the adsorption abilities of $\text{Cr}_2\text{O}_7^{2-}$ over $\text{H}_2\text{TCPP} \subset \text{Im-UiO-66}$ and $\text{H}_2\text{TCPP} \subset (\text{I}-)\text{Meim-UiO-66}$ were firstly studied before conducting the photocatalytic experiments. As expected, the cationic $\text{H}_2\text{TCPP} \subset (\text{I}-)\text{Meim-UiO-66}$ shows a higher adsorption rate and capacity than those of $\text{H}_2\text{TCPP} \subset \text{Im-UiO-66}$, which could be attributed to the ion exchange between I[−] and $\text{Cr}_2\text{O}_7^{2-}$ in $\text{H}_2\text{TCPP} \subset (\text{I}-)\text{Meim-UiO-66}$ (Fig. S4–6). It should also be noted that the protonation of pyrrole N in porphyrin ligands at acidic aqueous solution and the existence of Zr-OH/H₂O in the Zr₆ clusters can also enhance the adsorption of $\text{Cr}_2\text{O}_7^{2-}$ by both $\text{H}_2\text{TCPP} \subset \text{Im-UiO-66}$ and $\text{H}_2\text{TCPP} \subset (\text{I}-)\text{Meim-UiO-66}$ [36,37]. Interestingly, compared with our synthesized MOF materials, the typical visible light photocatalysts such as g-C₃N₄, Bi₂WO₆ show negligible $\text{Cr}_2\text{O}_7^{2-}$ adsorption performance, due to the lack of adsorption sites (Fig. S7–11).

Encouraged by the unique features including high adsorption rate and capacity for $\text{Cr}_2\text{O}_7^{2-}$ and strong visible-light absorption ability, the cationic multivariate MOF $\text{H}_2\text{TCPP} \subset (\text{I}-)\text{Meim-UiO-66}$ was then utilized for the photoreduction of $\text{Cr}_2\text{O}_7^{2-}$ under visible light. Previous studies revealed that the $\text{Cr}_2\text{O}_7^{2-}$ photoreduction rate could be enhanced at low pH values [7,8,21]. Thus, the photoreduction experiments were conducted at a pH of 2 and evaluated by monitoring the UV-vis spectra of diphenylcarbazide (DPC)-Cr₂O₇²⁻ solutions. Considering that most of the neutral porous MOFs have weak adsorption rates for $\text{Cr}_2\text{O}_7^{2-}$ and need relatively long time to achieve adsorption-desorption equilibrium, the one-hour dark equilibrium conditions (Fig. S4) were used before the photoreduction experiments for comparing their activity [6,7,20,21,24,25,38–41]. As shown in Fig. 2a, the control experiments showed that the photoreduction of $\text{Cr}_2\text{O}_7^{2-}$ to Cr³⁺ could not proceed in the absence of any catalyst. Furthermore, the Cr₂O₇²⁻ also could hardly be converted to Cr³⁺ without light irradiation, which indicated that the self-reduction of Cr₂O₇²⁻ can be precluded. In contrast, the reaction proceeded smoothly in the presence of the MOF photocatalysts under visible light irradiation (420 nm–780 nm). Nearly 70% of Cr₂O₇²⁻ can be reduced by Im-UiO-66 under visible light irradiation in half an hour. Interestingly, the reduction amount of Cr₂O₇²⁻ was enhanced dramatically and reached to 90% for $\text{H}_2\text{TCPP} \subset \text{Im-UiO-66}$ containing the highly photosensitive porphyrin units under the same conditions, which was ascribed to the fact that more electron-hole pairs were generated during light irradiation. More importantly, the ionized $\text{H}_2\text{TCPP} \subset (\text{I}-)\text{Meim-UiO-66}$ showed the highest activity (almost removed) among all the catalysts, which was attributed to the fact that the cationic framework can efficiently improve the adsorption of Cr₂O₇²⁻ and the utilization of the photoexcited electron. Notably, the counter anions I[−] in $\text{H}_2\text{TCPP} \subset (\text{I}-)\text{Meim-UiO-66}$ could also acted as sacrificial agent to increase the photoreduction activity. The complete conversion of Cr₂O₇²⁻ to Cr³⁺ can be proved by XPS data of $\text{H}_2\text{TCPP} \subset (\text{I}-)\text{Meim-UiO-66}$ after the photocatalysis process under the irradiation of visible light. As shown in Fig. 2b, the binding energy of 577.2 eV and 587.2 eV corresponded to Cr 2p_{3/2} and Cr 2p_{1/2} of Cr³⁺, respectively, which indicated that all the toxic Cr₂O₇²⁻ had been converted to environmental Cr³⁺ by the photoreduction reaction. To further evaluate their activities, the kinetics (Fig. 2c) of photoreduction of Cr₂O₇²⁻ were also calculated based on the data shown in Fig. 2a. The photoreduction of Cr₂O₇²⁻ follows pseudo-first-order kinetics, as verified by the linear plot of ln (C_e/C_t) vs. t, where C_e, C_t, K, and t are the concentration of Cr₂O₇²⁻ after one-hour equilibrium, the concentration of Cr₂O₇²⁻ after irradiation time t, the pseudo-first-order kinetics rate constant, and the reaction time, respectively. As shown in Fig. 2c, the photocatalyst $\text{H}_2\text{TCPP} \subset \text{Im}$

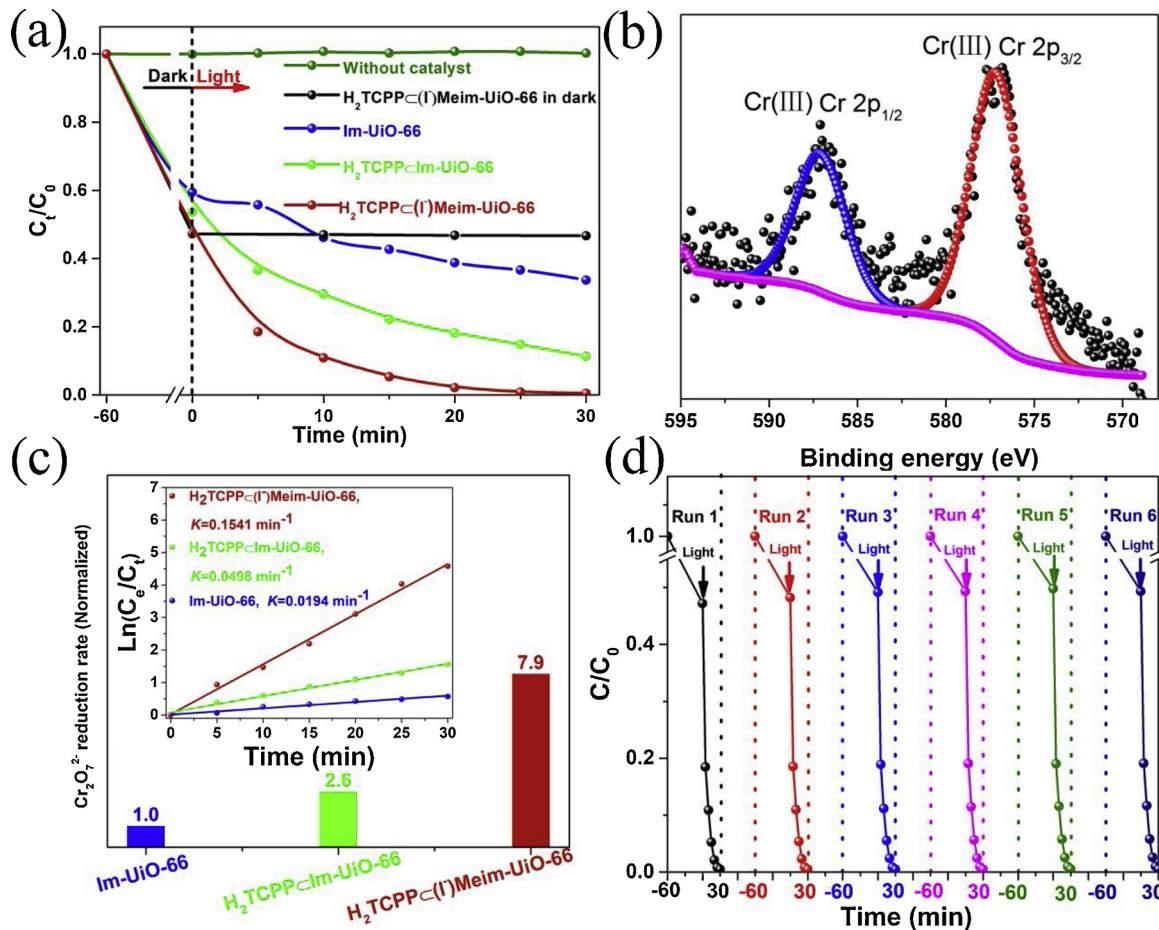


Fig. 2. a) The photoreduction of $\text{Cr}_2\text{O}_7^{2-}$ over Im-Uio-66, H₂TCPP C(I)-Im-Uio-66, and H₂TCPP C(I)-Meim-Uio-66 under visible light (420 nm–780 nm) and the reaction without catalyst or light. b) XPS plots of H₂TCPP C(I)-Meim-Uio-66 after $\text{Cr}_2\text{O}_7^{2-}$ photoreduction. c) Photoreduction rate of $\text{Cr}_2\text{O}_7^{2-}$ over Im-Uio-66, H₂TCPP C(I)-Im-Uio-66, and H₂TCPP C(I)-Meim-Uio-66, the inset picture shows the photoreduction kinetics of corresponding catalysts. d) the reusability of H₂TCPP C(I)-Meim-Uio-66 for the photoreduction of $\text{Cr}_2\text{O}_7^{2-}$ under visible light.

UiO-66 containing porphyrin units achieved a photocatalytic rate of 0.0498 min^{-1} , 2.6 times faster than that of the parent Im-Uio-66, which was attributed to the extended light absorption range. More interestingly, after ionization, the photoreduction rate of H₂TCPP C(I)-Meim-Uio-66 was further improved to 0.1541 min^{-1} , achieving a photoactivity 7.9 times higher than that of Im-Uio-66, which was ascribed to the strong adsorption of Cr(VI) and large range of visible-light photosensitivity. It should also be noted that H₂TCPP C(I)-Meim-Uio-66 achieved an rate of 22.7 and 5.0 times higher than porphyrin-based PCN-224 and amino-functionalized NH₂-UiO-66, respectively (Fig. S12–14) [38,42]. As far as we know, this is the best catalyst among all the reported MOF-based photocatalysts including typical NH₂-UiO-66 (0.2 mg_{Cr(VI)}/g_{catalyst}/min) and NH₂-MIL-125 (1.6 mg_{Cr(VI)}/g_{catalyst}/min) for Cr(VI) photoreduction under visible-light irradiation, in which the I- in our imidazolium functionalized MOF acts as sacrificial agent. (Table S1) [20,23]. The incorporation of H₂TCPP into H₂TCPP C(I)-Meim-Uio-66 can greatly enlarge the visible absorption range from 425 nm to 750 nm. To confirm its corresponding reactivity, action spectrum (wavelength dependence) measurements had also been conducted under 450 nm, 520 nm, or 600 nm light irradiation. Fig. S15 shows the kinetics of $\text{Cr}_2\text{O}_7^{2-}$ photoreduction over H₂TCPP C(I)-Meim-Uio-66 under 450 nm, 520 nm and 600 nm light irradiation, and Fig. S16 shows the action spectrum (wavelength-dependence) measurements photoreduction rate of $\text{Cr}_2\text{O}_7^{2-}$ over H₂TCPP C(I)-Meim-Uio-66, both of which indicated that the incorporation of H₂TCPP into H₂TCPP C(I)-Meim-Uio-66 indeed decrease the energy gap of this photocatalyst, and increase the photoreduction activity in visible range.

The photocatalytic reduction of $\text{Cr}_2\text{O}_7^{2-}$ by g-C₃N₄ and Bi₂WO₆ had been conducted under the same conditions. Only low photoreduction activity has been observed, which verify the good performance of H₂TCPP C(I)-Meim-Uio-66 (Fig. S17). Moreover, H₂TCPP C(I)-Meim-Uio-66 showed excellent chemical stability, which was verified by the recycle experiments and the PXRD patterns before and after the photoreduction of Cr(VI) (Figs. 2d and S18).

3.3. Clarification of the mechanism

The above results clearly demonstrated that the introduction of highly visible light photosensitive H₂TCPP units and strongly Cr(VI) adsorptive cationic struts into a multivariate MOF can obviously increase the activity of photoreduction of $\text{Cr}_2\text{O}_7^{2-}$. We then tried to understand the catalytic mechanism of the multivariate MOF. As we know, the band structure, the separation efficiency and transfer processes of photogenerated charge carries, and the $\text{Cr}_2\text{O}_7^{2-}$ adsorption could affect the photoreduction of efficiency $\text{Cr}_2\text{O}_7^{2-}$.

The band structures (conduction band (CB) and valence band (VB) positions) of H₂TCPP C(I)-Im-Uio-66 and H₂TCPP C(I)-Meim-Uio-66 were firstly studied using solid UV-vis DRS and Mott-Schottky plots. As shown in Fig. S19–21, the flat-band potential of H₂TCPP C(I)-Im-Uio-66 is determined to be -1.1 V versus Ag/AgCl at pH = 6.8, corresponding to ca. -0.9 V versus NHE, which is more negative than the $\text{Cr}_2\text{O}_7^{2-}/\text{Cr}^{3+}$ potential ($+0.51 \text{ V}$, pH = 6.8). [7] This finding indicated that H₂TCPP C(I)-Im-Uio-66 was a potential catalyst for the photocatalytic reduction of $\text{Cr}_2\text{O}_7^{2-}$. Compared with the parent H₂TCPP C(I)-Im-Uio-66,

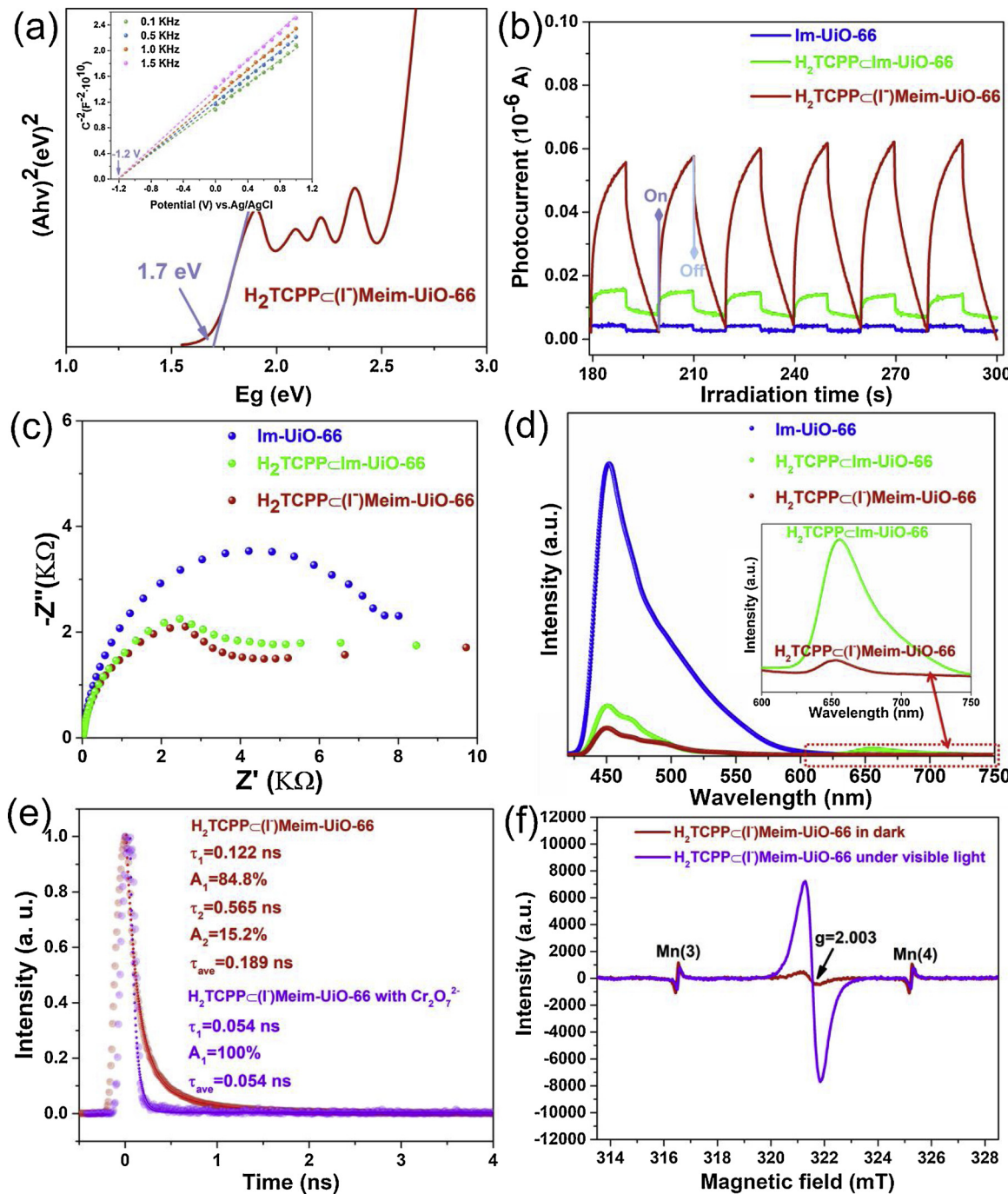


Fig. 3. a) Solid UV-vis absorption data (calculated from the reflectance using the Kubelka-Munk function) of $\text{H}_2\text{TCPP} \subset (\text{I}^-)\text{Meim-Uio-66}$, the inset picture in a) is Mott-Schottky plots of $\text{H}_2\text{TCPP} \subset (\text{I}^-)\text{Meim-Uio-66}$. b) Transient photocurrent responses of Im-Uio-66, $\text{H}_2\text{TCPP} \subset \text{Im-Uio-66}$, and $\text{H}_2\text{TCPP} \subset (\text{I}^-)\text{Meim-Uio-66}$ under visible light irradiation (420 nm–780 nm). c) EIS Nyquist plots of Im-Uio-66, $\text{H}_2\text{TCPP} \subset \text{Im-Uio-66}$ and $\text{H}_2\text{TCPP} \subset (\text{I}^-)\text{Meim-Uio-66}$; d) Steady-state PL spectrum of Im-Uio-66, $\text{H}_2\text{TCPP} \subset \text{Im-Uio-66}$ and $\text{H}_2\text{TCPP} \subset (\text{I}^-)\text{Meim-Uio-66}$ excited at 400 nm, the inset picture in d) shows the enlarge area between 600–750 nm. e) Time-resolved PL spectra of $\text{H}_2\text{TCPP} \subset (\text{I}^-)\text{Meim-Uio-66}$ and $\text{H}_2\text{TCPP} \subset (\text{I}^-)\text{Meim-Uio-66}$ containing $\text{Cr}_2\text{O}_7^{2-}$ suspensions at 650 nm emission ($\lambda_{\text{ex}} = 400$ nm). f) ESR analyses of $\text{H}_2\text{TCPP} \subset (\text{I}^-)\text{Meim-Uio-66}$ before and after visible light irradiation (420–780 nm), and Mn in the ESR tube as internal standard for ESR measurement.

the CB potential of $\text{H}_2\text{TCPP} \subset (\text{I}^-)\text{Meim-Uio-66}$ shows a negative drift with -0.1 V, which indicated that the ionized material is more favorable to photoreduce the $\text{Cr}_2\text{O}_7^{2-}$ (Figs. 3a and S21). Combining the results of solid UV-vis DRS and Mott-Schottky plots, the valence band of $\text{H}_2\text{TCPP} \subset \text{Im-Uio-66}$ and $\text{H}_2\text{TCPP} \subset (\text{I}^-)\text{Meim-Uio-66}$ can be calculated to be $+0.9$ V and $+0.7$ V, respectively. Thus, the $\text{Cr}_2\text{O}_7^{2-}/\text{Cr}^{3+}$ potential is straddled in the HOMO and LUMO energies of $\text{H}_2\text{TCPP} \subset \text{Im-Uio-66}$ and $\text{H}_2\text{TCPP} \subset (\text{I}^-)\text{Meim-Uio-66}$ (Fig. S21), indicating that the photogenerated electrons can easily transfer to the

adsorbed $\text{Cr}_2\text{O}_7^{2-}$, and the two photocatalysts are suitable for photo-reduction of $\text{Cr}_2\text{O}_7^{2-}$.

The separation efficiency of photogenerated charge carries in MOFs was then investigated by transient photocurrent measurements, electrochemical impedance spectroscopy (EIS), and steady-state photoluminescence (steady-state PL). As shown in Fig. 3b, Im-Uio-66 shows almost no transient photocurrent response (0.004 μA) under irradiation with visible light (420 nm–780 nm) due to its narrow light absorbing region. As expected, after the introduction of highly visible-light

sensitivity porphyrin units, the transient photocurrent response of $\text{H}_2\text{TCPP} \subset \text{Im}-\text{UiO}-66$ under visible light irradiation increased immediately ($0.016 \mu\text{A}$). Notably, after the ionization of precursor $\text{H}_2\text{TCPP} \subset \text{Im}-\text{UiO}-66$, the transient photocurrent response of $\text{H}_2\text{TCPP} \subset (\text{I}^-)\text{Meim}-\text{UiO}-66$ further increased, which was ascribed to the fact that the cationic MOF could be acted as ionic conductor to facilitate for the inhibition of the recombination of photogenerated electrons and holes [43,44]. Similar tendencies were also observed in EIS measurements. The results of EIS (Fig. 3c and Table S2) indicated that all of the as-prepared photocatalysts have the similar solution resistances (R_s) at $6.86 \pm 1.00 \Omega$. However, great changes in charge transfer resistances (R_{ct}) are observed after the incorporation of H_2TCPP . From the results of EIS, $\text{H}_2\text{TCPP} \subset \text{Im}-\text{UiO}-66$ containing H_2TCPP shows smaller R_{ct} value ($5.50 \text{ k}\Omega$), compared with $\text{Im}-\text{UiO}-66$ ($7.52 \text{ k}\Omega$). Interestingly, after ionization, the cationic $\text{H}_2\text{TCPP} \subset (\text{I}^-)\text{Meim}-\text{UiO}-66$ R_{ct} value ($5.47 \text{ k}\Omega$) was further decreased, which confirmed that the incorporation of porphyrin units and ionization indeed plays a significant role in the increasing interfacial charge transfer. This finding can be further confirmed by steady-state PL spectrum (Fig. 3d). Interestingly, the PL intensity obtained over $\text{H}_2\text{TCPP} \subset (\text{I}^-)\text{Meim}-\text{UiO}-66$ is much weaker than that of $\text{Im}-\text{UiO}-66$ and $\text{H}_2\text{TCPP} \subset \text{Im}-\text{UiO}-66$, thus indicating the faster electron transfer of photogenerated electrons and holes after incorporation of H_2TCPP and ionization.

To investigate the electron transfer processes in the photocatalyst during visible light irradiation, we then resorted to time-resolved PL spectra, a robust tool to track the photoexcited carrier. Here we firstly studied the electron transfer process originated from ligand H_2TCPP in $\text{H}_2\text{TCPP} \subset (\text{I}^-)\text{Meim}-\text{UiO}-66$. Fig. 3e shows the PL kinetics for $\text{H}_2\text{TCPP} \subset (\text{I}^-)\text{Meim}-\text{UiO}-66$ suspension with or without $\text{Cr}_2\text{O}_7^{2-}$ emitted at 650 nm ($\lambda_{ex} = 400 \text{ nm}$) (the emission spectrum at 650 nm is originated from H_2TCPP ligand). $\text{H}_2\text{TCPP} \subset (\text{I}^-)\text{Meim}-\text{UiO}-66$ shows two time constants, that is, $\tau_1 = 0.122 \text{ ns}$ (84.8%) and $\tau_2 = 0.565 \text{ ns}$ (15.2%). After the in-situ addition of $\text{Cr}_2\text{O}_7^{2-}$, the long lifetime constant disappeared, while the short lifetime constant decreased significantly from 0.122 ns to 0.054 ns , which indicated that long-lived electrons photogenerated by H_2TCPP can easily transfer to $\text{Cr}_2\text{O}_7^{2-}$. Similar result can also be obtained by comparing the PL kinetics for $\text{H}_2\text{TCPP} \subset \text{Im}-\text{UiO}-66$ suspensions with or without $\text{Cr}_2\text{O}_7^{2-}$ emitted at 650 nm ($\lambda_{ex} = 400 \text{ nm}$, Fig. S22–23). Thereafter we turned to study the electron transfer process originated from the ligand ($\text{I}^-)\text{Meim}-\text{H}_2\text{BDC}$ in ($\text{I}^-)\text{Meim}-\text{UiO}-66$ and $\text{H}_2\text{TCPP} \subset (\text{I}^-)\text{Meim}-\text{UiO}-66$. Fig. S24–25 show the PL kinetics for $(\text{I}^-)\text{Meim}-\text{UiO}-66$ and $\text{H}_2\text{TCPP} \subset (\text{I}^-)\text{Meim}-\text{UiO}-66$ at 455 nm emission ($\lambda_{ex} = 400 \text{ nm}$), respectively (the emission spectrum at 455 nm is originated from ($\text{I}^-)\text{Meim}-\text{H}_2\text{BDC}$ ligand). ($\text{I}^-)\text{Meim}-\text{UiO}-66$ presents two time constants of $\tau_1 = 0.111 \text{ ns}$ (81.1%) and $\tau_2 = 0.862 \text{ ns}$ (18.9%) with $\tau_{ave} = 0.253 \text{ ns}$, while $\text{H}_2\text{TCPP} \subset (\text{I}^-)\text{Meim}-\text{UiO}-66$ has only one time constant, that is, $\tau_1 = 0.109 \text{ ns}$ (100%). The decrement of the $\text{H}_2\text{TCPP} \subset (\text{I}^-)\text{Meim}-\text{UiO}-66$ PL lifetime could be ascribed to the fact that the energy transfer from ($\text{I}^-)\text{Meim}-\text{H}_2\text{BDC}$ linker to porphyrin which can increase the electron density on porphyrin linker (Figs. 1c and 3 d). The similar result can also be obtained by comparing $\text{Im}-\text{UiO}-66$ and $\text{H}_2\text{TCPP} \subset \text{Im}-\text{UiO}-66$ (Fig. S26–27). After in-situ addition of $\text{Cr}_2\text{O}_7^{2-}$ into the suspension of $\text{H}_2\text{TCPP} \subset (\text{I}^-)\text{Meim}-\text{UiO}-66$, the time constant nearly not changed (from 0.109 ns to 0.101 ns), implying that the lifetime of electrons generated by ($\text{I}^-)\text{Meim}-\text{H}_2\text{BDC}$ linker were too short to be used for photoreduction of $\text{Cr}_2\text{O}_7^{2-}$ (Fig. S28).

The electron transfer processes in photocatalysts were further studied by ESR analyses, which were conducted both in dark and under visible light irradiation under argon atmosphere. As shown in Figs. 3f and S29, after visible light irradiation, the ESR signals at $g = 2.003$ for both of $\text{H}_2\text{TCPP} \subset \text{Im}-\text{UiO}-66$ and $\text{H}_2\text{TCPP} \subset (\text{I}^-)\text{Meim}-\text{UiO}-66$ enhanced distinctly, indicating that the photogenerated electrons transferred from excited porphyrin to the Zr sites to form $(\text{Zr}^{3+}/\text{Zr}^{4+})_6\text{O}_4(\text{OH})_4$ in $\text{H}_2\text{TCPP} \subset (\text{I}^-)\text{Meim}-\text{UiO}-66$. However, the nearly unchanged ESR signal of $\text{Im}-\text{UiO}-66$ and $(\text{I}^-)\text{Meim}-\text{UiO}-66$ before and

after visible light irradiation may be attributed to their weak light absorption property (Fig. S30–31). Moreover, the ESR measurements conducted under air atmosphere revealed that the O_2^- species adsorbed on Zr^{3+} sites were produced under visible light irradiation (Fig. S32), which also indicates that the photogenerated electrons transfer from excited porphyrin to the Zr sites to form $(\text{Zr}^{3+}/\text{Zr}^{4+})_6\text{O}_4(\text{OH})_4$ [45].

To gain a deep insight for the generation and transfer processes of the charge carriers in photocatalysts, theoretical calculation for the electronic structures of $\text{H}_2\text{TCPP} \subset (\text{I}^-)\text{Meim}-\text{UiO}-66$ was conducted based on density functional theory (DFT) within a local density approximation (LDA) [46]. As shown in Fig. S33–36, the profiles of the weights of atomic orbitals' components [47] obtained by projecting the eigen wave functions onto the atomic orbitals indicate that the valence band maximum of $\text{H}_2\text{TCPP} \subset (\text{I}^-)\text{Meim}-\text{UiO}-66$ is mainly composed of C 2p and N 2p derived from porphyrin, while some unoccupied states of C 2p originating from porphyrin and ($\text{I}^-)\text{Meim}-\text{H}_2\text{BDC}$ linker are well hybridized with the unoccupied states of Zr_{4d} and the unoccupied states derived from C 2p of the ($\text{I}^-)\text{Meim}-\text{H}_2\text{BDC}$ linker are present at slightly lower part of the hybridized band. Conveniently, the unoccupied states of Cr_{3d} exists in the range of those bands. Therefore, the theoretical results demonstrated a favorable electron transfer from excited porphyrin to the Zr sites to form $(\text{Zr}^{3+}/\text{Zr}^{4+})_6\text{O}_4(\text{OH})_4$ in $\text{H}_2\text{TCPP} \subset (\text{I}^-)\text{Meim}-\text{UiO}-66$. The electron on Zr sites can also transfer to C 2p of the ($\text{I}^-)\text{Meim}-\text{H}_2\text{BDC}$ linker. If with the exist of $\text{Cr}_2\text{O}_7^{2-}$, the electrons on porphyrin units can easily transfer to the $\text{Cr}_2\text{O}_7^{2-}$ site directly or indirectly via Zr nodes and ($\text{I}^-)\text{Meim}-\text{H}_2\text{BDC}$ linker, thus suggest the photoreduction of the $\text{Cr}_2\text{O}_7^{2-}$ to Cr^{3+} . The location of the unoccupied band bottom was spanned by the Zr sites, and the unoccupied band of the linker ($\text{I}^-)\text{Meim}-\text{H}_2\text{BDC}$ is slightly lower than that of porphyrin, which can provide a great advantage for separation of the photo excited electron carrier and distributing the carrier to $\text{Cr}_2\text{O}_7^{2-}$ sites.

On the basis of the results from the above steady-state PL, time-resolved PL, EIS, photocurrent analysis, solid UV-vis spectra, Mott-Stocky analysis, XPS, ESR and theoretical calculation, a photoreduction mechanism of $\text{Cr}_2\text{O}_7^{2-}$ over $\text{H}_2\text{TCPP} \subset (\text{I}^-)\text{Meim}-\text{UiO}-66$ was proposed and is illustrated in Fig. 4. The anionic $\text{Cr}_2\text{O}_7^{2-}$ were firstly adsorbed by the protonated porphyrin, Zr-bond hydroxides, and methylated $\text{Im}-\text{H}_2\text{BDC}$ in porous cationic $\text{H}_2\text{TCPP} \subset (\text{I}^-)\text{Meim}-\text{UiO}-66$. Under the irradiation of the visible-light, the excited electrons on porphyrin units can easily transfer to the adsorbed $\text{Cr}_2\text{O}_7^{2-}$ anions directly or indirectly via Zr nodes and ($\text{I}^-)\text{Meim}-\text{H}_2\text{BDC}$ linker, which were then reduced to Cr^{3+} cations. On the other hand, the counter anions, I^- acted as hole scavengers to form I_2 in this photocatalytic reaction system, which was confirmed by XPS spectra (Fig. S37).

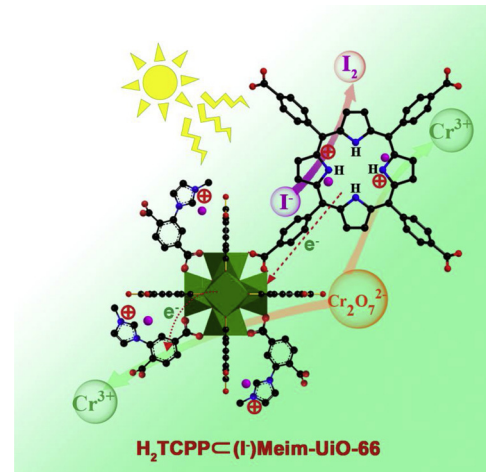


Fig. 4. Proposed mechanism for the photoreduction of $\text{Cr}_2\text{O}_7^{2-}$ to Cr^{3+} over $\text{H}_2\text{TCPP} \subset (\text{I}^-)\text{Meim}-\text{UiO}-66$ under visible light irradiation.

4. Conclusions

In conclusion, a multivariate metal organic framework, H₂TCP*C*(I⁻)Meim-UiO-66, with the integration of intense visible-light absorption porphyrin unit and strong Cr₂O₇²⁻ adsorption cationic strut, was fabricated via a sequential mixed-ligand and ionization strategy. The introduction of highly photosensitive porphyrin units into the MOF nanocrystals effectively expanded the spectral response from 425 to 750 nm. The cationic struts in the H₂TCP*C*(I⁻)Meim-UiO-66 could effectively enhance the adsorption of anionic Cr₂O₇²⁻ due to the electrostatic effect. The synergistic effect of the strong adsorption of Cr₂O₇²⁻ and the efficient utilization of visible-light endowed H₂TCP*C*(I⁻)Meim-UiO-66 with highly efficient photoreduction activity toward Cr₂O₇²⁻ under visible light in a rate of 13.3 mg_{Cr(VI)}/g_{catalyst}/min, much higher than the reported MOF-based photocatalysts including typical NH₂-UiO-66 (0.2 mg_{Cr(VI)}/g_{catalyst}/min) and NH₂-MIL-125 (1.6 mg_{Cr(VI)}/g_{catalyst}/min). Based on the results from time-resolved photoluminescence spectra, electron spin resonance, and theoretical calculation etc., a photoreduction mechanism of Cr₂O₇²⁻ over H₂TCP*C*(I⁻)Meim-UiO-66 was also well proposed. Our findings provide a strategy to design higher efficient photocatalytic materials.

Acknowledgements

We gratefully acknowledge the financial support of the National Key Research and Development Program of China (2018YFA0208600, 2017YFA0700100), Key Research Program of Frontier Science, CAS (QYZDJ-SSW-SLH045), Strategic Priority Research Program of the Chinese Academy of Sciences (XDB20000000), NSFC (21671188, 21871263, 21520102001 and 21331006), Youth Innovation Promotion Association, CAS (2014265) and China Scholarship Council (201704910486). We also show our great thanks to Mr. Qi Wang for providing Bi₂WO₆ as control catalyst.

Appendix A. Supplementary data

Supplementary material related to this article can be found, in the online version, at doi:<https://doi.org/10.1016/j.apcatb.2019.04.074>.

References

- [1] N.R. Bishnoi, M. Bajaj, N. Sharma, A. Gupta, Bioresour. Technol. 91 (2004) 305–307.
- [2] C.-C. Wang, X.-D. Du, J. Li, X.-X. Guo, P. Wang, J. Zhang, Appl. Catal. B: Environ. 193 (2016) 198–216.
- [3] H.-L. Ma, Y. Zhang, Q.-H. Hu, D. Yan, Z.-Z. Yu, M. Zhai, J. Mater. Chem. 22 (2012) 5914–5916.
- [4] K.C.K. Lai, I.M.C. Lo, Environ. Sci. Technol. 42 (2008) 1238–1244.
- [5] A.U. Chaudhari, S.R. Tapase, V.L. Markad, K.M. Kodam, J. Hazard. Mater. 262 (2013) 580–588.
- [6] R. Liang, F. Jing, L. Shen, N. Qin, L. Wu, J. Hazard. Mater. 287 (2015) 364–372.
- [7] F. Jing, R. Liang, J. Xiong, R. Chen, S. Zhang, Y. Li, L. Wu, Appl. Catal. B: Environ. 206 (2017) 9–15.
- [8] R. Liang, L. Shen, F. Jing, W. Wu, N. Qin, R. Lin, L. Wu, Appl. Catal. B: Environ. 162 (2015) 245–251.
- [9] Y.B. Huang, J. Liang, X.S. Wang, R. Cao, Chem. Soc. Rev. 46 (2017) 126–157.
- [10] K. Yuan, T. Song, D. Wang, X. Zhang, X. Gao, Y. Zou, H. Dong, Z. Tang, W. Hu, Angew. Chem. Int. Ed. 130 (2018) 5810–5815.
- [11] S. Wang, X. Wang, Angew. Chem. Int. Ed. 55 (2016) 2308–2320.
- [12] H. Zhang, J. Wei, J. Dong, G. Liu, L. Shi, P. An, G. Zhao, J. Kong, X. Wang, X. Meng, J. Zhang, J. Ye, Angew. Chem. Int. Ed. 55 (2016) 14310–14314.
- [13] M. Zhao, K. Yuan, Y. Wang, G. Li, J. Guo, L. Gu, W. Hu, H. Zhao, Z. Tang, Nature 539 (2016) 76–80.
- [14] X.S. Wang, L. Li, D.Q. Yuan, Y.B. Huang, R. Cao, J. Hazard. Mater. 344 (2017) 283–290.
- [15] Y.B. Huang, Q. Wang, J. Liang, X. Wang, R. Cao, J. Am. Chem. Soc. 138 (2016) 10104–10107.
- [16] X.S. Wang, J. Liang, L. Li, Z.J. Lin, P.P. Bag, S.Y. Gao, Y.B. Huang, R. Cao, Inorg. Chem. 55 (2016) 2641–2649.
- [17] T. Zhang, W. Lin, Chem. Soc. Rev. 43 (2014) 5982–5993.
- [18] Y. Fang, Y. Ma, M. Zheng, P. Yang, A.M. Asiri, X. Wang, Coord. Chem. Rev. 373 (2018) 83–115.
- [19] C. Xu, H. Liu, D. Li, J.H. Su, H.L. Jiang, Chem. Sci. 9 (2018) 3152–3158.
- [20] L. Shen, R. Liang, M. Luo, F. Jing, L. Wu, Phys. Chem. Chem. Phys. 17 (2015) 117–121.
- [21] L. Shi, T. Wang, H. Zhang, K. Chang, X. Meng, H. Liu, J. Ye, Adv. Sci. 2 (2015) 1500006.
- [22] Y. Gu, Y.N. Wu, L. Li, W. Chen, F. Li, S. Kitagawa, Angew. Chem. Int. Ed. 56 (2017) 15658–15662.
- [23] H. Wang, X. Yuan, Y. Wu, G. Zeng, X. Chen, L. Leng, Z. Wu, L. Jiang, H. Li, J. Hazard. Mater. 280 (2015) 187–194.
- [24] L. Shen, W. Wu, R. Liang, R. Lin, L. Wu, Nanoscale 5 (2013) 9374–9382.
- [25] R. Liang, F. Jing, L. Shen, N. Qin, L. Wu, Nano Res. 8 (2015) 3237–3249.
- [26] X. Wang, J. Liu, S. Leong, X. Lin, J. Wei, B. Kong, Y. Xu, Z.-X. Low, J. Yao, H. Wang, ACS Appl. Mater. Inter. 8 (2016) 9080–9087.
- [27] H. Deng, C.J. Doonan, H. Furukawa, R.B. Ferreira, J. Towne, C.B. Knobler, B. Wang, O.M. Yaghi, Science 327 (2010) 846–850.
- [28] J. Pang, S. Yuan, J. Qin, M. Wu, C.T. Lollar, J. Li, N. Huang, B. Li, P. Zhang, H.C. Zhou, J. Am. Chem. Soc. 140 (2018) 12328–12332.
- [29] J. Liang, Y.Q. Xie, Q. Wu, X.Y. Wang, T.T. Liu, H.F. Li, Y.B. Huang, R. Cao, Inorg. Chem. 57 (2018) 2584–2593.
- [30] Y. Sun, L. Sun, D. Feng, H.C. Zhou, Angew. Chem. Int. Ed. 55 (2016) 6471–6475.
- [31] J.H. Cavka, S. Jakobsen, U. Olsbye, N. Guillou, C. Lamberti, S. Bordiga, K.P. Lillerud, J. Am. Chem. Soc. 130 (2008) 13850–13851.
- [32] A.V. Desai, B. Manna, A. Karmakar, A. Sahu, S.K. Ghosh, Angew. Chem. Int. Ed. 55 (2016) 7811–7815.
- [33] J. Liang, R.-P. Chen, X.-Y. Wang, T.-T. Liu, X.-S. Wang, Y.-B. Huang, R. Cao, Chem. Sci. 8 (2017) 1570–1575.
- [34] H. Wu, Y.S. Chua, V. Krungleviciute, M. Tyagi, P. Chen, T. Yildirim, W. Zhou, J. Am. Chem. Soc. 135 (2013) 10525–10532.
- [35] C.A. Trickett, K.J. Gagnon, S. Lee, F. Gandara, H.B. Burgi, O.M. Yaghi, Angew. Chem. Int. Ed. 54 (2015) 11162–11167.
- [36] A.J. Howarth, M.J. Katz, T.C. Wang, A.E. Platero-Prats, K.W. Chapman, J.T. Hupp, O.K. Farha, J. Am. Chem. Soc. 137 (2015) 7488–7494.
- [37] S. Yuan, J.S. Qin, L. Zou, Y.P. Chen, X. Wang, Q. Zhang, H.C. Zhou, J. Am. Chem. Soc. 138 (2016) 6636–6642.
- [38] L. Shen, S. Liang, W. Wu, R. Liang, L. Wu, Dalton Trans. 42 (2013) 13649–13657.
- [39] R. Liang, L. Shen, F. Jing, N. Qin, L. Wu, ACS Appl. Mater. Inter. 7 (2015) 9507–9515.
- [40] R. Liang, R. Chen, F. Jing, N. Qin, L. Wu, Dalton Trans. 44 (2015) 18227–18236.
- [41] L. Shen, L. Huang, S. Liang, R. Liang, N. Qin, L. Wu, RSC Adv. 4 (2014) 2546–2549.
- [42] D. Feng, W.C. Chung, Z. Wei, Z.Y. Gu, H.L. Jiang, Y.P. Chen, D.J. Daresbourg, H.C. Zhou, J. Am. Chem. Soc. 135 (2013) 17105–17110.
- [43] X. Fang, Q. Shang, Y. Wang, L. Jiao, T. Yao, Y. Li, Q. Zhang, Y. Luo, H.L. Jiang, Adv. Mater. 30 (2018) 1705112.
- [44] P. Zhang, M. Li, B. Yang, Y. Fang, X. Jiang, G.M. Veith, X.G. Sun, S. Dai, Adv. Mater. 27 (2015) 8088–8094.
- [45] J. Long, S. Wang, Z. Ding, S. Wang, Y. Zhou, L. Huang, X. Wang, Chem. Commun. 48 (2012) 11656–11658.
- [46] J.P. Perdew, A. Zunger, Phys. Rev. B 23 (1981) 5048–5079.
- [47] M. Oshikiri, J. Ye, M. Boero, J. Phys. Chem. C 118 (2014) 8331–8341.